

Generation of Weyl points and a nodal line by magnetization reorientation in $\text{Co}_3\text{Sn}_2\text{S}_2$

F. Schilberth,^{1,2} M.-C. Jiang,^{3,4} F. Le Mardel⁵, L. B. Papp,² I. Mohelsky,⁵ M. A. Kassem,^{6,7} Y. Tabata,⁶ T. Waki,⁶ H. Nakamura,⁶ G.-Y. Guo,^{3,8} M. Orlita,^{5,9} R. Arita,^{4,10} I. Kézsmárki,¹ and S. Bordács^{1,2,11}

¹*Experimentalphysik V, Center for Electronic Correlations and Magnetism, Institute for Physics, Augsburg University, D-86135 Augsburg, Germany*

²*Department of Physics, Institute of Physics, Budapest University of Technology and Economics, Műegyetem rkp. 3., H-1111 Budapest, Hungary*

³*Department of Physics and Center for Theoretical Physics, National Taiwan University, Taipei 10617, Taiwan*

⁴*RIKEN Center for Emergent Matter Science, 2-1 Hirosawa, Wako 351-0198, Japan**

⁵*Laboratoire National des Champs Magnétiques Intenses, LNCMI-EMFL, CNRS UPR3228, Univ. Grenoble Alpes, Univ. Toulouse, Univ. Toulouse 3, INSA-T, Grenoble and Toulouse, France*

⁶*Department of Materials Science and Engineering, Kyoto University, Kyoto 606-8501, Japan*

⁷*Department of Physics, Faculty of Science, Assiut University, 71516 Assiut, Egypt*

⁸*Physics Division, National Center for Theoretical Sciences, Taipei 10617, Taiwan*

⁹*Faculty of Mathematics and Physics, Charles University, Ke Karlovu 5, Prague, 121 16, Czech Republic*

¹⁰*Department of Physics, University of Tokyo, 7-3-1 Hongo Bunkyo-ku, Tokyo, 113-0033, Japan*

¹¹*HUN-REN-BME Condensed Matter Physics Research Group, Budapest University of Technology and Economics, Műegyetem rkp. 3., H-1111 Budapest, Hungary†*

(Dated: August 8, 2024)

Topological magnets exhibit fascinating properties like topologically protected surface states or anomalous transport phenomena. While these properties can be significantly altered by manipulating the magnetic state, the experimental verification of such predictions remains challenging. Here, we demonstrate the efficient magnetic field control of the Weyl semimetallic state of the collinear ferromagnet $\text{Co}_3\text{Sn}_2\text{S}_2$ by magneto-optical spectroscopy. We resolve a redshift of the nodal loop resonance as the magnetization is rotated into the kagome plane by the magnetic field. Our material-specific theory, capturing the observed field-induced spectral reconstruction, shows the creation of 26 Weyl points for one in-plane magnetization direction and predicts the emergence of a gapless nodal loop for the orthogonal in-plane magnetization orientation. These findings demonstrate that while topological band structures are generally considered robust, breaking underlying crystal symmetries with external fields provides an efficient way to manipulate them, even in collinear magnets. This approach opens exciting avenues to control band topology also in materials with more complex magnetic structures and even to study the interplay of real- and momentum-space topological states, e.g. in skyrmion-lattice systems.

I. INTRODUCTION

The interpretation of the quantum Hall, the anomalous Hall and the quantum spin Hall effects based on momentum space topology, has fostered the development of a new field, the study of topological phases in condensed matter [1–3]. These theoretical efforts eventually culminated in the formulation of a periodic table of gapped and gapless topological phases depending on the dimensionality and symmetry class of the system [4]. While some of these phases still remain theoretical predictions, a number of intriguing topological states have already been experimentally confirmed in recent years, among them topological insulators, Dirac and Weyl semimetals [5–7]. It was proposed that the interplay between magnetism and topology fundamentally shapes the band structure through symmetries determined by the magnetic order. Therefore, the non-trivial band topology and its magnetic control may allow us to realize unusual electronic phenomena and phases such as the (quantum) anomalous Hall- and Nernst-effects, and spin-momentum locked surface states, making these magnets compelling for ap-

plications in spintronics and quantum information technology [8, 9].

While several theoretical studies indeed predict that magnetic fields can create or annihilate Weyl nodes and move their position in the band structure [10–13], experimental demonstrations of these effects are scarce. Magnetotransport experiments suggest the transformation of a nodal ring to a Weyl-semimetallic phase in EuP_3 [14] and in Co_2MnAl [15], whereas Shubnikov-de-Haas oscillations propose a field-induced reconstruction of the Fermi surface in $\text{Co}_3\text{Sn}_2\text{S}_2$ [16]. In addition, it was shown for the nodal planes in MnSi that linear band crossings occur only on k -planes parallel to an applied magnetic field [17]. While these examples prove that indeed the band structure in topological magnets can be highly sensitive to the magnetic state, they also highlight the difficulties of magnetotransport and magnetometry experiments to provide direct band-specific information. While spectroscopy may help to overcome these challenges, perhaps the only spectroscopic study on the magnetic control of band topology so far are scanning tunneling spectroscopy results of Yin *et al.* which imply a reconstruction of massive Dirac bands upon the rotation of a magnetic field in the kagome metal Fe_3Sn_2 [18]. Due to the shortcoming of other spectroscopic methods in magnetic fields (the incompatibility or angular resolved photoemission spectroscopy with external fields and the technical limitation of

* ming-chun.jiang@riken.jp

† bordacs.sandor@tk.bme.hu

scanning tunneling spectroscopy to moderate magnetic fields), here we use magneto-optical spectroscopy to reveal the magnetic field control of the band topology in $\text{Co}_3\text{Sn}_2\text{S}_2$ up to 34 T.

As a proof of this concept, here we investigate the evolution of the nodal lines in $\text{Co}_3\text{Sn}_2\text{S}_2$ by measuring magneto-reflectance upon the gradual rotation of the magnetization from the c axis to two perpendicular directions in the kagome plane. We observe a strong redshift of the previously reported giant magneto-optical resonance [19] upon this magnetization re-orientation. As only few bands lie around the Fermi energy, our material-specific theory can unambiguously reveal the origin of this shift: Due to the lower symmetry of the in-plane magnetized case, various Weyl nodes emerge by closing the spin-orbit coupling (SOC) induced gap at specific k points or even recover a continuous gapless nodal line, depending on the orientation of the magnetization within the kagome plane. In addition, we show that the spin-orbit gap changes differently for the two symmetry-inequivalent types of nodal loops. Our showcase study provides a deep insight into the mechanism of magnetically driven reconstructions of electronic band topology.

Here, we choose the archetypical magnetic Weyl semimetal $\text{Co}_3\text{Sn}_2\text{S}_2$ due to its simple band structure close to the Fermi level. The crystal structure is built up by kagome layers of Co stacked along the c axis in an ABC -fashion. Below $T_C \approx 177$ K, it becomes a collinear ferromagnet with magnetic moments pointing along the stacking direction [20], while anomalies in the susceptibility just below T_C are attributed to domain wall transitions [21, 22]. Magnetization measurements reveal extraordinarily large uniaxial anisotropy, where fields as high as 23 T are required to fully turn the magnetization into the kagome plane [23]. Nonrelativistic density functional theory (DFT) calculations predicted nodal loops, located around the Fermi energy on high symmetry planes of the Brillouin zone (BZ), which are gapped by SOC except for six Weyl points [24]. Angular resolved photoemission studies confirmed the existence of the nodal line and traced its evolution across the magnetic transition [25]. In the paramagnetic state, these results suggest the existence of a 4-fold degenerate Dirac loop, which upon breaking time-reversal by the magnetic order is split into two Weyl loops of opposite spin polarisation. One of them moves to higher energies upon increasing magnetic moment, while its partner stays close to the Fermi energy and was shown to be responsible for large anomalous Hall effect, Nernst effect and magneto-optical activity [13, 19, 24–27]. These results indicate that the topological band structure features are strongly coupled to the magnetic order in this kagome metal.

II. RESULTS AND DISCUSSION

A. Symmetry analysis

In order to motivate our detailed experimental and *ab initio* studies, first we consider the modification of symmetries upon the field-induced magnetization reorientation. For the ground state magnetization $\mathbf{M} \parallel c$, all nodal loops are equivalent due

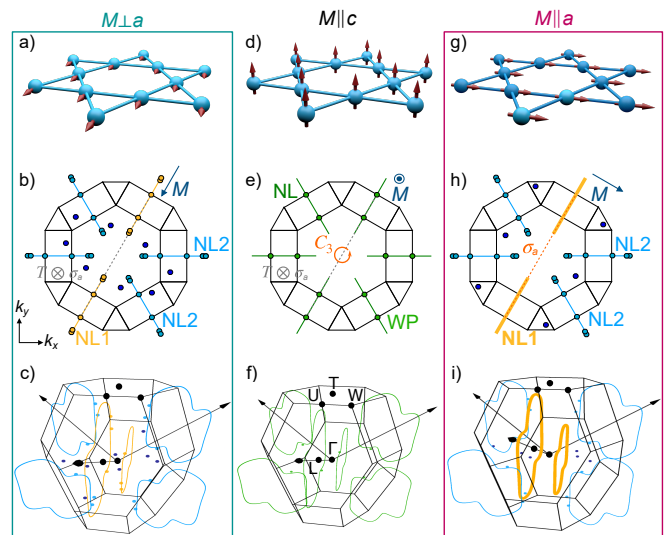


FIG. 1. Symmetries and topology for out-of- and in-plane magnetic field in $\text{Co}_3\text{Sn}_2\text{S}_2$. The first row (a, d, g) shows a real-space representation of the magnetization for $\mathbf{M} \perp a$, $\mathbf{M} \parallel c$ and $\mathbf{M} \parallel a$. The second and third rows show a top and 3D view of the corresponding BZ for the respective configuration. (a–c) Emerging Weyl points (WP) for $\mathbf{M} \perp a$. The in-plane magnetization makes the gapped nodal loops inequivalent (NL1/2) and produces additional Weyl points. Those have the same color as their corresponding loop or are dark blue if located at other k points. The mirror symmetry σ_a has to be combined with time-reversal T . (d–f) Three equivalent nodal loops related by the C_3 rotational symmetry for out-of-plane magnetization. (g–i) Inequivalent nodal loops for $\mathbf{M} \parallel a$. For this configuration, the mirror plane σ_a is a symmetry and protects the nodal loop NL1 (thick yellow) from being gapped.

to the C_3 rotational symmetry, as shown in Fig. 1(d–f). In contrast, for magnetization in the kagome plane, the 3-fold rotational symmetry is broken, leaving mirror symmetries when the axial vector of the magnetic moment is perpendicular to the mirror plane. Therefore, for $\mathbf{M} \parallel a$, this results in the magnetic point group $C2'/m$, which hosts a mirror plane σ_a . As shown in Fig. 1(g–i), this plane contains a nodal loop NL1, which will therefore be protected from being gapped by SOC (thick yellow). The remaining loops, NL2 (light blue) are related by the mirror operation, but are not protected, hence they are gapped except for 6 Weyl points on each loop. Additionally, we find 6 Weyl points away from the nodal lines (dark blue). So in total we obtain 18 Weyl points and a protected nodal loop in the BZ. For the perpendicular in-plane direction $\mathbf{M} \perp a$, shown in panels (a–c), we obtain a similar situation. However, in this case, the magnetic point group is $C2'/m'$, e.g. the mirror plane is a symmetry only in combination with time-reversal. As this does not protect a pair of loops (NL1), these are gapped to 6 Weyl points by SOC. The remaining loops are again related by this operation and gapped to 6 Weyl points. Here we find 8 additional Weyl points away from the loops, so we obtain a total of 26 Weyl points distributed in the BZ. While some of these features were predicted earlier [13, 28], a direct experimental investigation of field-induced reconstruction of band topology has been lacking. Along this line, the central

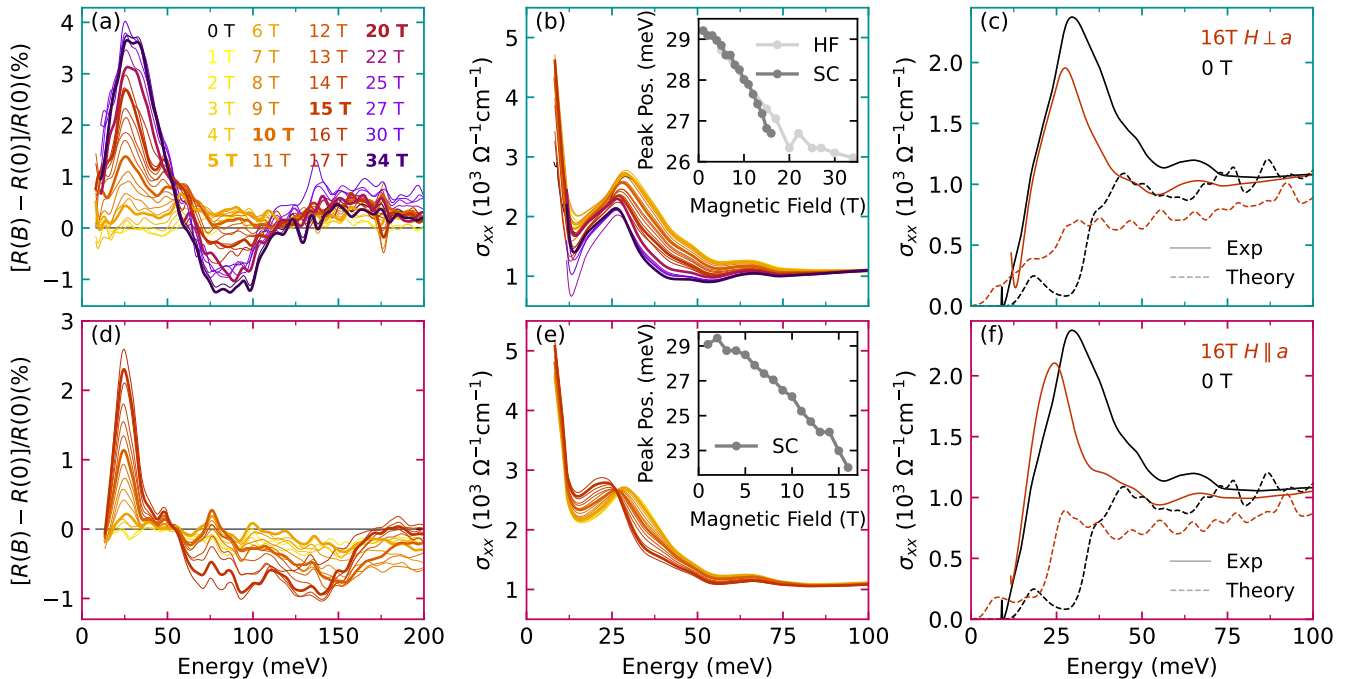


FIG. 2. Magneto-reflectance data measured for fields up to 34 T. (a, d) Raw magneto-reflectance data $[R(B) - R(0)]/R(0)$ for $\mathbf{H} \perp a$ and $\mathbf{H} \parallel a$, respectively (b, e) Optical conductivity in field calculated from the zero-field reflectivity of Ref. 19 and the magneto-reflectance data for both in-plane field orientations. The insets show the evolution of the 29 meV peak as a function of the field for the merged datasets from experiments in a resistive magnet (HF) and superconducting solenoid (SC). (c, f) Comparison of the zero-field and high-field conductivities with *ab initio* calculations for both field directions.

question of this work is whether changes in the nodal lines and the emergence of additional Weyl nodes can be resolved by optical spectroscopy. Additionally, a very recent theoretical study by Nakazawa *et al.* [29] developed for kagome monolayers, predicts an anisotropy of the band structure for different in-plane directions of the magnetization which manifests in magnetotransport and as we show also in optical properties of bulk crystals.

B. Magneto-optical spectroscopy

Fig. 2(a) and (d) show magneto-reflectance spectra over the energy range of 12-200 meV in different magnetic fields applied in the kagome plane along and perpendicular to the a axis, respectively. Due to the limited measurement time at the high-field (HF) facility, the spectra for the latter configuration could only be collected in a superconducting (SC) setup up to 16 T. For both configurations, we obtain similar magneto-reflectance spectra, $[R(B) - R(0)]/R(0)$, although the detailed lineshapes are slightly different. With increasing magnetic field, a peak develops at low energies, followed by a minimum at the high-energy side. For $\mathbf{H} \perp a$, these two features are centered around 29 meV and 85 meV, while for $\mathbf{H} \parallel a$ the peak is shifted to lower energies and the minimum broadens considerably. For both configurations, the magneto-reflectance vanishes towards higher energies, indicating that field-induced band reconstructions are limited to the $\lesssim 200$ meV vicinity of

the Fermi energy.

The detailed field dependence of the low-energy peak for the two directions is shown in Fig. E1 for the SC and HF datasets, where error bars are determined from the noise level of the spectra. For $\mathbf{H} \perp a$ in panel (a), the magnitude increases up to 22 T and then saturates, following the same behaviour as the magnetization for in-plane fields [23]. The field dependence of the peak for $\mathbf{H} \parallel a$ is shown in panel (b), resulting in the same trend and similar magnitude up to 16 T. For $\mathbf{H} \perp a$, the additional spectral weight due to this peak pushes the reflectivity very close to 1 for high fields, as shown in Fig. E2. The observed changes with a peak magnitude of 3.7% at 34 T can therefore be considered remarkably large for an itinerant magnet.

In order to quantify and interpret the magnetic field-induced changes of the band structure, we calculate the field dependence of the optical conductivity. The corresponding spectra are shown in Fig. 2(b) and (e) for the two field directions, exhibiting a very similar behaviour in magnetic field. The most prominent features are the tail of the Drude response dominating the spectra below 15 meV and a peak around 29 meV, which shifts to smaller energies at higher fields. The position of the latter as a function of the field is shown in the respective inset. It again follows the same trend as the magnetization for both in-plane field directions, although the magnitude of the shift is larger for $\mathbf{H} \parallel a$.

As demonstrated in Ref. 19, this peak is caused by transitions between bands associated with the partially gapped nodal

lines, that can be excited almost exclusively by one of the two circular polarization states of light. In panels (c) and (f), the spectra measured at 0 T (magnetization along c) and 16 T (magnetization almost in plane), after subtraction of the Drude contribution, are compared to the spectra obtained from *ab initio* calculations for the two magnetic configurations. The theory spectra reproduce the experimental features on a broad energy scale (compare Ref. 19). The shift of the nodal line resonance is captured well as the onset of optical weight appears at lower energies for both directions of the in-plane fields, though the peak in the theory spectra is not as pronounced as in the experiment. The difference may be caused by electronic correlations [30], or the magnitude of the matrix elements for these transitions may be underestimated by the theory. We directly compare the calculated optical conductivity for different in-plane orientations of the magnetic field in Fig. E3. The in-plane spectra are very similar at high energies but show small differences around the resonance at 30 meV. While for $\mathbf{M} \parallel a$ the slope of the peak is shifted parallel compared to the $\mathbf{M} \parallel c$ spectrum, the peak for $\mathbf{M} \perp a$ is broadened and the slope reduced. In addition the redshift is larger for $\mathbf{M} \parallel a$. All of these observations are consistent with the experimental data measured for the two directions.

C. *Ab initio* analysis

In order to evaluate the origin of the peak shift, we directly compare the band structures for the in- and out-of-plane configurations. Here, we only show the $\mathbf{M} \parallel a$ case with the protected nodal line, while the analysis for $\mathbf{M} \perp a$ can be found in Fig. E4 which yields very similar conclusions. For $\mathbf{M} \parallel c$, all low-energy band touchings lie on the high symmetry plane of the BZ and all nodal loops are equivalent, we therefore focus on one representative loop (Fig. 1(e-f)). However, magnetization along two orthogonal directions in the kagome plane, along or perpendicular to a pair of loops (NL1), leads to two different types of nodal lines as shown in Fig. 1(b-c) and (h-i) respectively, governed by the mirror symmetry. The other two pairs of loops (NL2) have a perpendicular component with respect to the magnetization. For $\mathbf{M} \parallel a$, NL1 stays protected by the mirror symmetry even with SOC, while NL2 breaks up into 6 Weyl points each and we find 6 additional Weyl nodes at other k -points (dark blue).

Firstly, we compare the differences between the nodal lines. Fig. 3(a-c) plot the gap size of the loops for $\mathbf{M} \parallel c$, NL1 and NL2 for $\mathbf{M} \parallel a$ respectively. The position of Weyl points is shown in red and the Fermi surface with dark green lines. For both in-plane loops in panels (b) and (c), the average gap size is smaller than for out-of-plane magnetization in panel (a), not only for the protected loop. This is clearly reflected in the band structure plot in panel (g), where we show the bands for $\mathbf{M} \parallel c$ and $\mathbf{M} \parallel a$ in green and red, respectively. Along $A - B$ and $C - D$, the gapless nature of NL1 is highlighted, while the gap for NL2 is also smaller than for the bands with $\mathbf{M} \parallel c$.

Due to the smaller gap, these nodal lines contribute in a different energy range to the optical conductivity. Therefore, in panel (d), we plot the spectral weight distribution for out-

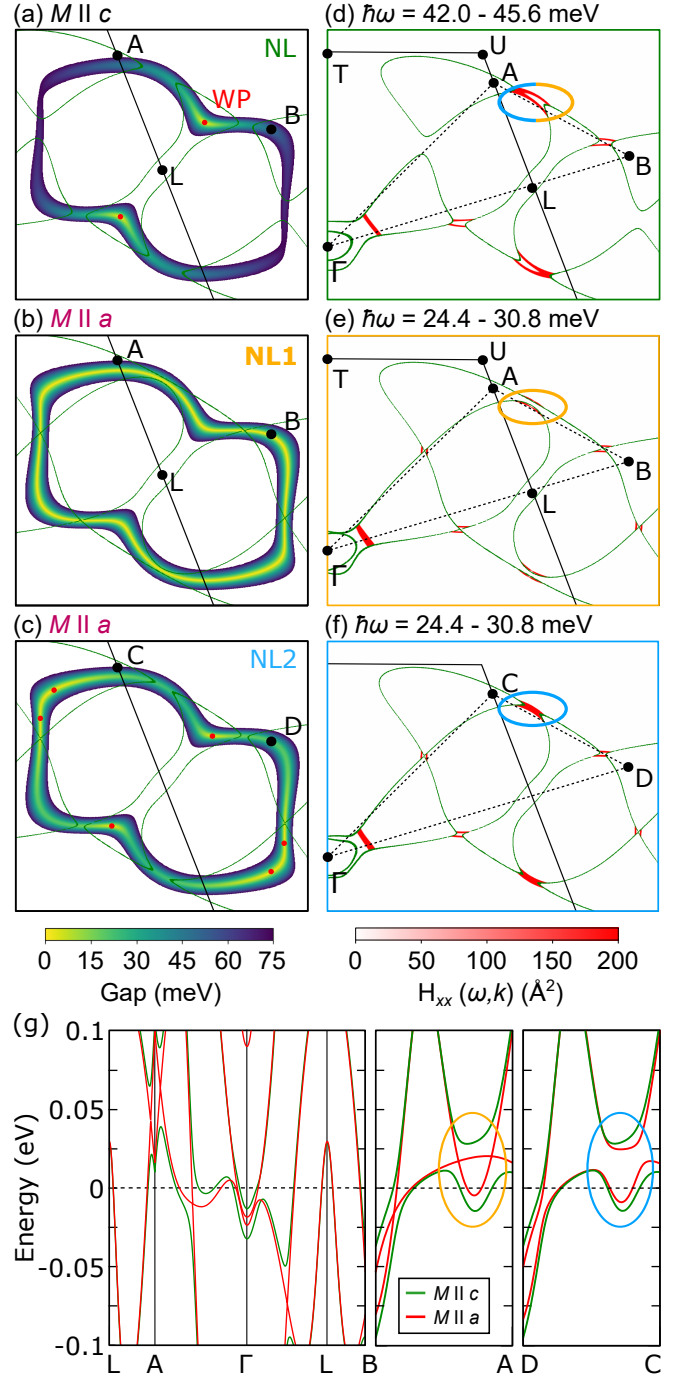


FIG. 3. Evolution of the nodal loop upon reorienting the magnetization to $\mathbf{M} \parallel a$. (a-c) gap of the nodal lines for out-of-plane and NL1 and NL2 in-plane loops, respectively. For (a), the average gap is larger than for (b) and (c). Points C and D are equivalent to A and B but lie on the BZ planes that contain NL2 instead of NL1. (d-f) Optical weight H_{xx} at the peak energies (42.0-45.6 meV in (d), 24.4-30.8 meV in (e) and (f)) distributed on the high symmetry planes of the BZ containing the nodal loops from (a-c). We obtain qualitatively similar distributions despite the different energy ranges. (g) band structure along the triangles in the right column. The high symmetry points are shown above and in Fig. 1(f). For NL1 the crossings are protect, while also for NL2, the SOC gap along the nodal line is clearly smaller than for out-of-plane.

of-plane magnetization at a photon energy of 42 - 45.6 meV, whereas for in-plane field in (e) and (f) we show the optical weight at 24.4 - 30.8 meV. Qualitatively, all plots show similar features with a small hotspot along $\Gamma - L$ and several hotspots where the nodal lines lie around the Fermi energy, e.g. on the $A - B$ and $C - D$ lines. This comparison shows that the onset of optical weight of the optical conductivity for in- and out-of-plane magnetization is generated by the same band structure regions, but at different photon energies, explaining the redshift of the peak observed as the moments cant into the kagome plane. For the $\mathbf{M} \perp a$ case in Fig. E4, the spectral weight is plotted at energies between 28.8 - 33.6 meV, also explaining the redshift found for this configuration, although it is smaller than for $\mathbf{M} \parallel a$ which is also observed by the experiment.

Interestingly, if we infer the position of the Weyl nodes from the left column with the gap energy plots in Figs. 3 and E4, we do not find any optical weight associated with transitions around these points for either magnetization direction. As was shown previously for $\mathbf{M} \parallel c$, the Weyl nodes are located around 60 meV above the Fermi level and therefore cannot contribute to the low-energy optical response [19]. For in-plane fields, while the gap changes significantly, the energy of the crossing point with respect to the Fermi level does not change upon reorientation of the magnetization. Therefore, the same argument also accounts for the absence of optical weight from the Weyl points for in-plane field.

Let us now discuss the possible origin of the nodal line reconstruction. Since the gap is initially produced by SOC, it has the same nature as the orbital magnetic moment [31] or the magnetocrystalline anisotropy [32, 33]. The origin of such anisotropy can be explained through the relative SOC strength by comparing the SOC matrix elements in the p - [33] or the d -orbital basis [34]. For the same spin channel, the SOC matrix elements $\langle d_{yz} | H_{\text{SOC}} | d_{xy, x^2-y^2} \rangle$ and $\langle d_{yz} | H_{\text{SOC}} | d_{z^2} \rangle$ prefer the in-plane anisotropy and $\langle d_{xy} | H_{\text{SOC}} | d_{x^2-y^2} \rangle$ and $\langle d_{yz} | H_{\text{SOC}} | d_{xz} \rangle$ prefer the out-of-plane anisotropy with the magnitude ratio being $\langle d_{yz} | H_{\text{SOC}} | d_{xy, x^2-y^2} \rangle^2 : \langle d_{yz} | H_{\text{SOC}} | d_{z^2} \rangle^2 : \langle d_{xy} | H_{\text{SOC}} | d_{x^2-y^2} \rangle^2 : \langle d_{yz} | H_{\text{SOC}} | d_{xz} \rangle^2 = 1 : 3 : 4 : 1$ [34]. Fig. E5 shows the projected band structures of $\text{Co}_3\text{Sn}_2\text{S}_2$ without the SOC. We notice that the nodal lines consist mainly of Co d_{xy, x^2-y^2} orbitals with less contributions from the Co $d_{xz, yz}$ orbitals. Thus, from the above relation, we note that the SOC matrix element of $\langle d_{xy} | H_{\text{SOC}} | d_{x^2-y^2} \rangle$ dominates, which vanishes for in-plane spin orientation. This not only implies that out-of-plane magnetism is energetically preferred but also the SOC strength is weaker when in-plane field is applied. Hence, we observe a gap shrink for in-plane magnetization in $\text{Co}_3\text{Sn}_2\text{S}_2$.

In summary, we presented a detailed magneto-optical study to monitor the reconstruction of the topological band structure in a prominent kagome magnet upon manipulation of the magnetic order by high external fields. We find that in $\text{Co}_3\text{Sn}_2\text{S}_2$, a low-energy resonance associated with a transition between bands of the nodal lines is highly susceptible to in-plane fields, leading to an energy shift as the magnetization cants into the ab plane. Our material specific theory is able to reproduce this shift and shows that as the SOC strength is reduced by the in-plane magnetization, the SOC induced gap of the nodal line is also reduced, shifting the resonance

in the optical conductivity. In particular, a complete degenerate nodal line emerges for $\mathbf{M} \parallel a$. Compared to quantum oscillation or STM measurements, this direct access to the interband response highlights the unique capabilities of optical spectroscopy to monitor changes in the band structure between different magnetic states, which may also be applied to study the band structures between metamagnetic phases of noncollinear systems or spin-chiral orders such as skyrmion lattices. Finally, we note that quantities probing Berry curvature, like the anomalous Hall effect or the magneto-optical Kerr effect could also be sensitive for the magnetic field induced changes in the band topology. As the dimension of the degenerate manifolds increases from Weyl points for $\mathbf{M} \perp a$ to loops for $\mathbf{M} \parallel a$, we expect an enhancement of the Hall response and reconstruction of the Hall spectral weight at finite frequencies. Following the changes in the topology of the bulk band structure, surface states may be also restructured. Since the nodal loop stays intact for $\mathbf{M} \parallel a$, we expect the formation of a drumhead surface state spanning the projection of NL1 on the surface, instead of the Fermi arcs present between the isolated Weyl points. The magnetization reorientation therefore provides an exciting pathway to study these exotic surface states, also applicable to other materials.

III. METHODS

A. Experimental Details

We carried out magneto-reflectance experiments on the same ab cut crystal which was used in a previous magneto-optical study [19]. Relative magneto-reflectance spectra, $[R(B) - R(0)]/R(0)$ were collected in Voigt configuration with the field aligned perpendicular to the in-plane a crystal axis, where $R(0)$ is the zero field and $R(B)$ is the finite field reflectivity spectrum. The light of a glabar was analyzed by a Bruker Vertex 80v Fourier-transform spectrometer in the energy range between 12 and 500 meV and guided to the sample position by a light-pipe. The sample was cooled to 4 K and placed in a superconducting coil (SC) for measurements up to 16 T and in a resistive magnet for high field measurements (HF) up to 34 T. The reflected light was collected and guided onto an external bolometer after passing a silicon beamsplitter. Due to the different optical path lengths in the SC and HF experiments, the raw signal was smaller in the high-field data in the overlapping field range. In order to compare the two datasets, the HF data was scaled with the corresponding SC data set at 5 and 10 T, whereas for 15 T and higher fields, the 15 T SC data was used for scaling. Therefore, the presented data for high fields shows a lower limit for the actual magnitude of the magnetic field-induced changes. To calculate the optical conductivity in field, we multiply the smoothed magneto-reflectance spectra with the 10 K zero-field reflectivity spectrum from Ref. 19 and perform a Kramers Kronig analysis with the same parameters as in the earlier work (see Fig. E2).

B. DFT calculations

The calculations of the electronic structures are conducted using DFT as implemented in the Vienna ab initio simulation package (VASP) [35, 36]. All the calculations are performed using the projector-augmented wave (PAW) [37] pseudopotential with the generalized gradient approximation (GGA) in the form of Perdew-Burke-Ernzerhof (PBE) [38, 39]. A plane-wave cutoff value of 400 eV and a Γ -centered $16 \times 16 \times 16$ k -mesh is used to describe the electronic structure. The valence orbital set is $4s^2 3d^7$ for Co, $5s^2 5p^2$ for Sn, and $3s^2 3p^4$ for S, respectively. For the crystal structure, we use the experimental lattice parameters, $a = 5.379$ Å and $\alpha = 59.8658^\circ$ [40]. Based on the DFT electronic band structures, we construct the Wannier functions using Co d , Sn s , p , and S s , p orbitals. Finally, the optical properties are evaluated using the Kubo-Greenwood formula under the Wannier interpolation [41]. A fine mesh of $200 \times 200 \times 200$ k points is applied during the integration with good convergence.

The optical conductivity given in Fig. 2(c) and the deduced spectral weight of certain photon energies plotted in Fig. 3

can be calculated through the Brillouin zone integration of the transition matrix elements:

$$\begin{aligned} \text{Re} \sigma_{\alpha\beta}(\hbar\omega) &= \frac{-\pi\omega e^2}{\hbar} \int_{\text{BZ}} \sum_{nm} f_{mn}^{\text{FD}} A_{nm,\alpha} A_{nm,\beta} \delta(\omega_{mn} - \omega) \\ &= \frac{-\pi\omega e^2}{\hbar} \int_{\text{BZ}} H_{\alpha\beta}(\hbar\omega) \end{aligned} \quad (1)$$

α and β are the indices in Cartesian coordinates, f_n^{FD} is the Fermi-Dirac distribution of band n , $f_{mn}^{\text{FD}} = f_m^{\text{FD}} - f_n^{\text{FD}}$, $\hbar\omega_{mn} = \hbar\omega_m - \hbar\omega_n$ is the energy difference between bands m and n . Finally, $A_{nm,\alpha} = \langle u_{n,k} | i\nabla_{k\alpha} | u_{m,k} \rangle$ is the Berry connection and $H_{\alpha\beta}(\hbar\omega)$ is the spectral weight at certain transition energy.

C. Data availability

The datasets generated during and/or analysed during the current study are available from the corresponding author on reasonable request.

-
- [1] D. J. Thouless, M. Kohmoto, M. P. Nightingale, and M. den Nijs, Quantized Hall Conductance in a Two-Dimensional Periodic Potential, *Physical Review Letters* **49**, 405 (1982).
- [2] N. Nagaosa, J. Sinova, S. Onoda, A. H. MacDonald, and N. P. Ong, Anomalous Hall effect, *Reviews of Modern Physics* **82**, 1539 (2010).
- [3] M. König, H. Buhmann, L. W. Molenkamp, T. Hughes, C.-X. Liu, X.-L. Qi, and S.-C. Zhang, The Quantum Spin Hall Effect: Theory and Experiment, *Journal of the Physical Society of Japan* **77**, 031007 (2008).
- [4] C.-K. Chiu, J. C. Teo, A. P. Schnyder, and S. Ryu, Classification of topological quantum matter with symmetries, *Reviews of Modern Physics* **88**, 035005 (2016).
- [5] C.-Z. Chang, J. Zhang, X. Feng, J. Shen, Z. Zhang, M. Guo, K. Li, Y. Ou, P. Wei, L.-L. Wang, Z.-Q. Ji, Y. Feng, S. Ji, X. Chen, J. Jia, X. Dai, Z. Fang, S.-C. Zhang, K. He, Y. Wang, L. Lu, X.-C. Ma, and Q.-K. Xue, Experimental observation of the quantum anomalous hall effect in a magnetic topological insulator, *Science* **340**, 167 (2013).
- [6] Z. K. Liu, B. Zhou, Y. Zhang, Z. J. Wang, H. M. Weng, D. Prabhakaran, S.-K. Mo, Z. X. Shen, Z. Fang, X. Dai, Z. Hussain, and Y. L. Chen, Discovery of a Three-Dimensional Topological Dirac Semimetal, Na_3Bi , *Science* **343**, 864 (2014).
- [7] B. Q. Lv, H. M. Weng, B. B. Fu, X. P. Wang, H. Miao, J. Ma, P. Richard, X. C. Huang, L. X. Zhao, G. F. Chen, Z. Fang, X. Dai, T. Qian, and H. Ding, Experimental Discovery of Weyl Semimetal TaAs, *Physical Review X* **5**, 031013 (2015).
- [8] M. J. Gilbert, Topological electronics, *Communications Physics* **4**, 1 (2021).
- [9] M. Z. Hasan and C. L. Kane, Colloquium : Topological insulators, *Reviews of Modern Physics* **82**, 3045 (2010).
- [10] A. A. Burkov and L. Balents, Weyl Semimetal in a Topological Insulator Multilayer, *Physical Review Letters* **107**, 127205 (2011).
- [11] C. J. Tabert and J. P. Carbotte, Optical conductivity of weyl semimetals and signatures of the gapped semimetal phase transition, *Physical Review B* **93**, 085442 (2016).
- [12] C. Fang, H. Weng, X. Dai, and Z. Fang, Topological nodal line semimetals, *Chinese Physics B* **25**, 1 (2016).
- [13] M. P. Ghimire, J. I. Facio, J.-S. You, L. Ye, J. G. Checkelsky, S. Fang, E. Kaxiras, M. Richter, and J. van den Brink, Creating Weyl nodes and controlling their energy by magnetization rotation, *Physical Review Research* **1**, 032044 (2019).
- [14] A. H. Mayo, H. Takahashi, M. S. Bahramy, A. Nomoto, H. Sakai, and S. Ishiwata, Magnetic Generation and Switching of Topological Quantum Phases in a Trivial Semimetal α - EuP_3 , *Physical Review X* **12**, 011033 (2022).
- [15] P. Li, J. Koo, W. Ning, J. Li, L. Miao, L. Min, Y. Zhu, Y. Wang, N. Alem, C.-X. Liu, Z. Mao, and B. Yan, Giant room temperature anomalous Hall effect and tunable topology in a ferromagnetic topological semimetal Co_2MnAl , *Nature Communications* **11**, 3476 (2020).
- [16] L. Ye, J. I. Facio, M. P. Ghimire, M. K. Chan, J.-S. You, D. C. Bell, M. Richter, J. v. d. Brink, and J. G. Checkelsky, *Field-dependent Shubnikov-de Haas oscillations in ferromagnetic Weyl semimetal $\text{Co}_3\text{Sn}_2\text{S}_2$* (2022).
- [17] M. A. Wilde, M. Dodenhöft, A. Niedermayr, A. Bauer, M. M. Hirschmann, K. Alpin, A. P. Schnyder, and C. Pfleiderer, Symmetry-enforced topological nodal planes at the Fermi surface of a chiral magnet, *Nature* **594**, 374 (2021).
- [18] J.-x. Yin, S. S. Zhang, H. Li, K. Jiang, G. Chang, B. Zhang, B. Lian, C. Xiang, I. Belopolski, H. Zheng, T. A. Cochran, S.-y. Xu, G. Bian, K. Liu, T.-r. Chang, H. Lin, Z.-y. Lu, Z. Wang, S. Jia, W. Wang, and M. Z. Hasan, Giant and anisotropic many-body spin-orbit tunability in a strongly correlated kagome magnet, *Nature* **562**, 91 (2018).
- [19] F. Schilberth, M.-C. Jiang, S. Minami, M. A. Kassem, F. Mayr, T. Koretsune, Y. Tabata, T. Waki, H. Nakamura, G.-Y. Guo, R. Arita, I. Kézsmárki, and S. Bordács, Nodal-line resonance generating the giant anomalous Hall effect of $\text{Co}_3\text{Sn}_2\text{S}_2$, *Physical Review B* **107**, 214441 (2023).

- [20] M. Zabel, S. Wandinger, and K.-J. Range, Ternary chalcogenides $M_3M'_2X_2$ with Shandite-type structure, *Z. Naturforsch.* **34b**, 238 (1979).
- [21] M. A. Kassem, Y. Tabata, T. Waki, and H. Nakamura, Low-field anomalous magnetic phase in the kagome-lattice Shandite $Co_3Sn_2S_2$, *Physical Review B* **96**, 014429 (2017).
- [22] C. Lee, P. Vir, K. Manna, C. Shekhar, J. E. Moore, M. A. Kastner, C. Felser, and J. Orenstein, Observation of a phase transition within the domain walls of ferromagnetic $Co_3Sn_2S_2$, *Nature Communications* **13**, 6 (2022).
- [23] J. Shen, Q. Zeng, S. Zhang, W. Tong, L. Ling, C. Xi, Z. Wang, E. Liu, W. Wang, G. Wu, and B. Shen, On the anisotropies of magnetization and electronic transport of magnetic Weyl semimetal $Co_3Sn_2S_2$, *Applied Physics Letters* **115**, 212403 (2019).
- [24] Q. Wang, Y. Xu, R. Lou, Z. Liu, M. Li, Y. Huang, D. Shen, H. Weng, S. Wang, and H. Lei, Large intrinsic anomalous Hall effect in half-metallic ferromagnet $Co_3Sn_2S_2$ with magnetic Weyl fermions, *Nature Communications* **9**, 3681 (2018).
- [25] I. Belopolski, T. A. Cochran, X. Liu, Z.-J. Cheng, X. P. Yang, Z. Guguchia, S. S. Tsirkin, J.-X. Yin, P. Vir, G. S. Thakur, S. S. Zhang, J. Zhang, K. Kaznatcheev, G. Cheng, G. Chang, D. Multer, N. Shumiya, M. Litskevich, E. Vescovo, T. K. Kim, C. Cacho, N. Yao, C. Felser, T. Neupert, and M. Z. Hasan, Signatures of Weyl Fermion Annihilation in a Correlated Kagome Magnet, *Physical Review Letters* **127**, 256403 (2021).
- [26] S. Minami, F. Ishii, M. Hirayama, T. Nomoto, T. Koretsune, and R. Arita, Enhancement of the transverse thermoelectric conductivity originating from stationary points in nodal lines, *Physical Review B* **102**, 205128 (2020).
- [27] Y. Okamura, S. Minami, Y. Kato, Y. Fujishiro, Y. Kaneko, J. Ikeda, J. Muramoto, R. Kaneko, K. Ueda, V. Kocsis, N. Kanazawa, Y. Taguchi, T. Koretsune, K. Fujiwara, A. Tsukazaki, R. Arita, Y. Tokura, and Y. Takahashi, Giant magneto-optical responses in magnetic Weyl semimetal $Co_3Sn_2S_2$, *Nature Communications* **11**, 4619 (2020).
- [28] A. Ozawa and K. Nomura, Two-orbital effective model for magnetic weyl semimetal in kagome-lattice shandite, *Journal of the Physical Society of Japan* **88**, 123703 (2019).
- [29] K. Nakazawa, Y. Kato, and Y. Motome, Topological transitions by magnetization rotation in kagome monolayers of ferromagnetic Weyl semimetal Co-based shandite, *arXiv*, 1 (2024).
- [30] Y. Xu, J. Zhao, C. Yi, Q. Wang, Q. Yin, Y. Wang, X. Hu, L. Wang, E. Liu, G. Xu, L. Lu, A. A. Soluyanov, H. Lei, Y. Shi, J. Luo, and Z.-G. Chen, Electronic correlations and flattened band in magnetic Weyl semimetal candidate $Co_3Sn_2S_2$, *Nature Communications* **11**, 3985 (2020).
- [31] G. Y. Guo and H. Ebert, Theoretical investigation of the orientation dependence of the magneto-optical Kerr effect in Co, *Phys. Rev. B* **50**, 10377 (1994).
- [32] D.-S. Wang, R. Wu, and A. J. Freeman, First-principles theory of surface magnetocrystalline anisotropy and the diatomic-pair model, *Phys. Rev. B* **47**, 14932 (1993).
- [33] M.-C. Jiang and G.-Y. Guo, Large magneto-optical effect and magnetic anisotropy energy in two-dimensional metallic ferromagnet Fe_3GeTe_2 , *Phys. Rev. B* **105**, 014437 (2022).
- [34] H. Takayama, K.-P. Bohnen, and P. Fulde, Magnetic surface anisotropy of transition metals, *Phys. Rev. B* **14**, 2287 (1976).
- [35] G. Kresse and J. Furthmüller, Efficiency of ab-initio total energy calculations for metals and semiconductors using a plane-wave basis set, *Computational Materials Science* **6**, 15 (1996).
- [36] G. Kresse and J. Furthmüller, Efficient iterative schemes for ab initio total-energy calculations using a plane-wave basis set, *Phys. Rev. B* **54**, 11169 (1996).
- [37] P. E. Blöchl, Projector augmented-wave method, *Phys. Rev. B* **50**, 17953 (1994).
- [38] J. P. Perdew, M. Ernzerhof, and K. Burke, Rationale for mixing exact exchange with density functional approximations, *The Journal of Chemical Physics* **105**, 9982 (1996).
- [39] G. Kresse and D. Joubert, From ultrasoft pseudopotentials to the projector augmented-wave method, *Phys. Rev. B* **59**, 1758 (1999).
- [40] P. Vaqueiro and G. G. Sobany, A powder neutron diffraction study of the metallic ferromagnet $Co_3Sn_2S_2$, *Solid State Sciences* **11**, 513 (2009).
- [41] G. Pizzi, V. Vitale, R. Arita, S. Blügel, F. Freimuth, G. Géranton, M. Gibertini, D. Gresch, C. Johnson, T. Koretsune, J. Ibañez-Azpiroz, H. Lee, J.-M. Lihm, D. Marchand, A. Marrazzo, Y. Mokrousov, J. I. Mustafa, Y. Nohara, Y. Nomura, L. Paulatto, S. Poncé, T. Ponweiser, J. Qiao, F. Thöle, S. S. Tsirkin, M. Wierzbowska, N. Marzari, D. Vanderbilt, I. Souza, A. A. Mostofi, and J. R. Yates, Wannier90 as a community code: new features and applications, *Journal of Physics: Condensed Matter* **32**, 165902 (2020).

ACKNOWLEDGMENTS

This work was supported by the Hungarian National Research, Development and Innovation Office NKFIH Grants No. FK 135003 and by the Ministry of Innovation and Technology and the National Research, Development and Innovation Office within the Quantum Information National Laboratory of Hungary, by the National Science and Technology Council in Taiwan, by the IPA program of RIKEN, Japan and by the Deutsche Forschungsgemeinschaft (DFG, German Research Foundation) – TRR 360 – 492547816.

IV. AUTHOR INFORMATION

A. Authors and Affiliations

B. Contributions

M.A.K., Y.T., T.W. and H.N. synthesized and characterized the crystals; F.S. measured the zero-field reflectivity; F.S., F.L., L.B.P., I.M., M.O. and S.B. performed the magnetoreflectance experiments. M.C.J., G.Y.G. and R.A. performed the *ab initio* calculations; F.S., M.C.J. and S.B. wrote the paper; I.K. and S.B. planned and coordinated the project. All authors contributed to the discussion and interpretation of the experimental and theoretical results and to the completion of the paper.

C. Corresponding author

Correspondence to Sándor Bordács on the magnetoreflectance experiments or to Ming-Chun Jiang for the DFT calculations.

V. ETHICS DECLARATIONS

A. Competing interests

The authors declare no competing interests.

EXTENDED DATA

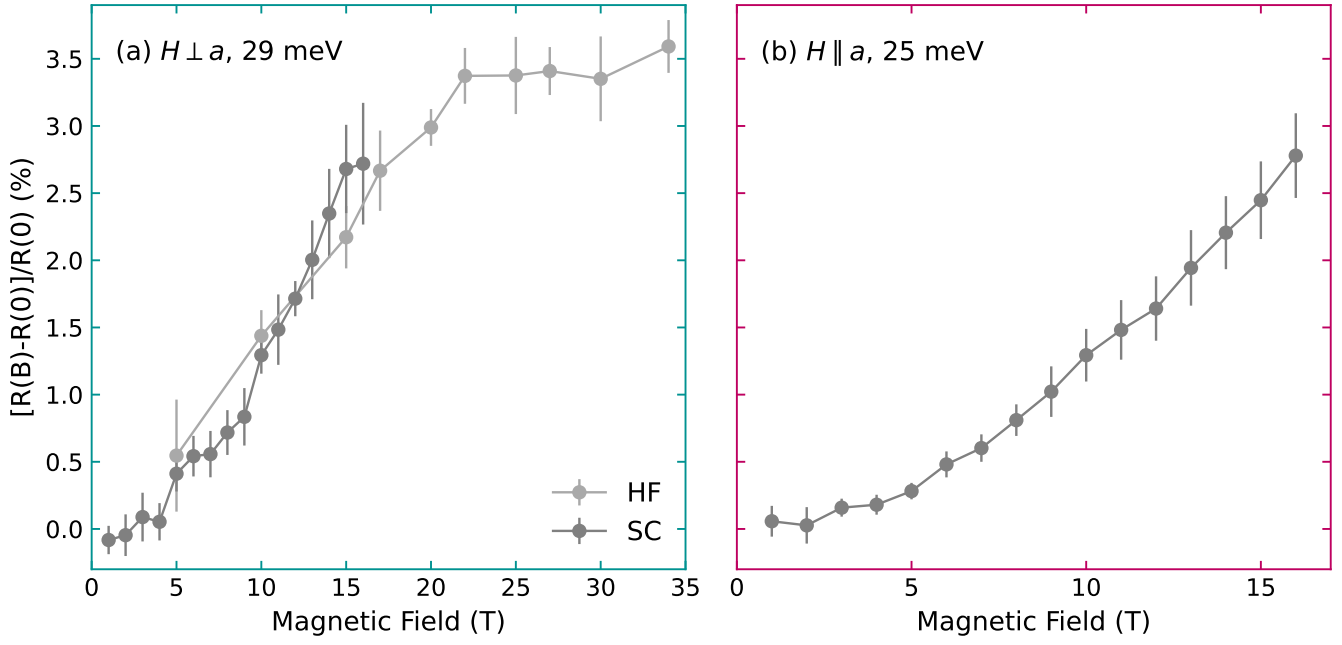


FIG. E1. (a,b) Magnitude of the peak at 29 meV for $\mathbf{H} \perp a$ and 25 meV for $\mathbf{H} \parallel a$ as function of field, respectively

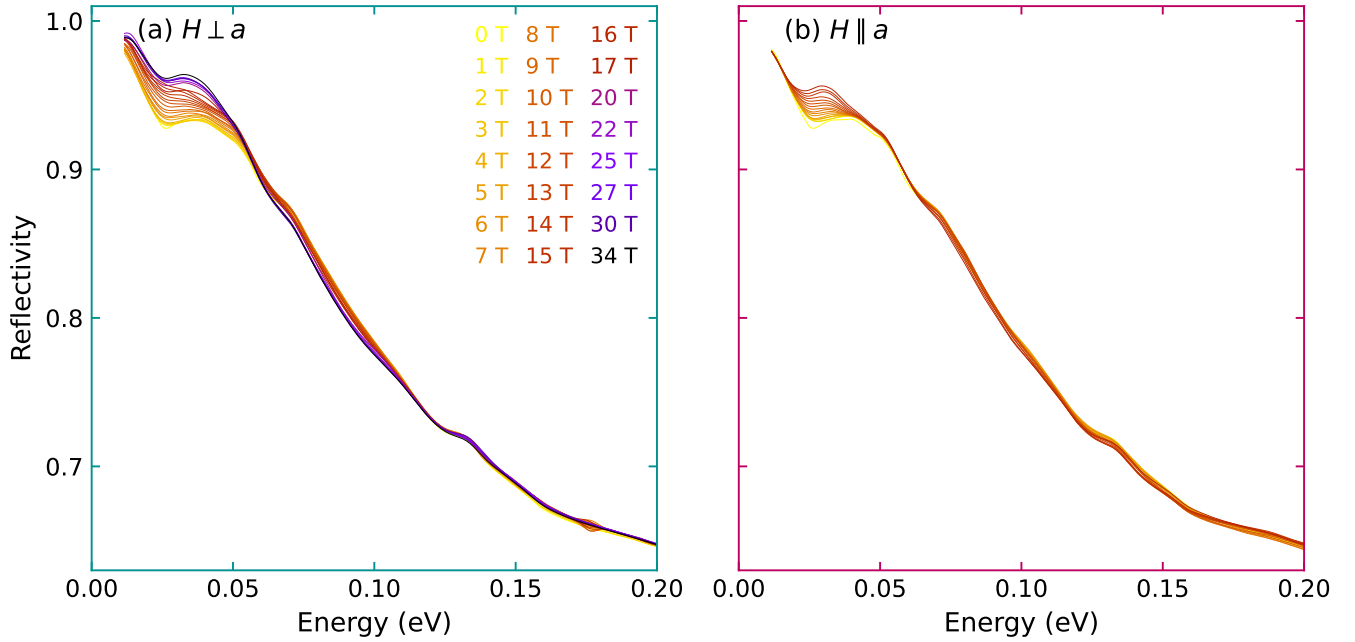


FIG. E2. Field dependent reflectivity spectra generated by multiplying the magnetorefectance data onto the 10 K spectrum of Ref. 19. Panels (a)&(b) show the spectra for $\mathbf{H} \perp a$ and $\mathbf{H} \parallel a$ as function of field, respectively

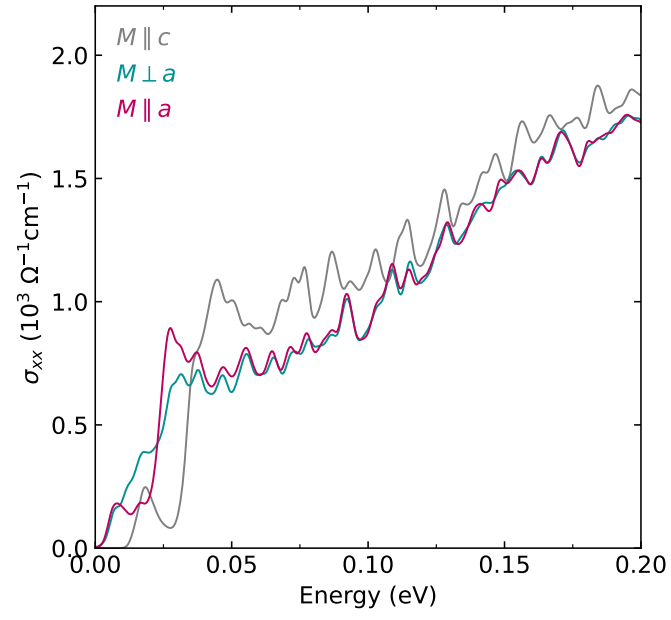


FIG. E3. Comparison of the calculated in plane and out of plane optical conductivity spectra

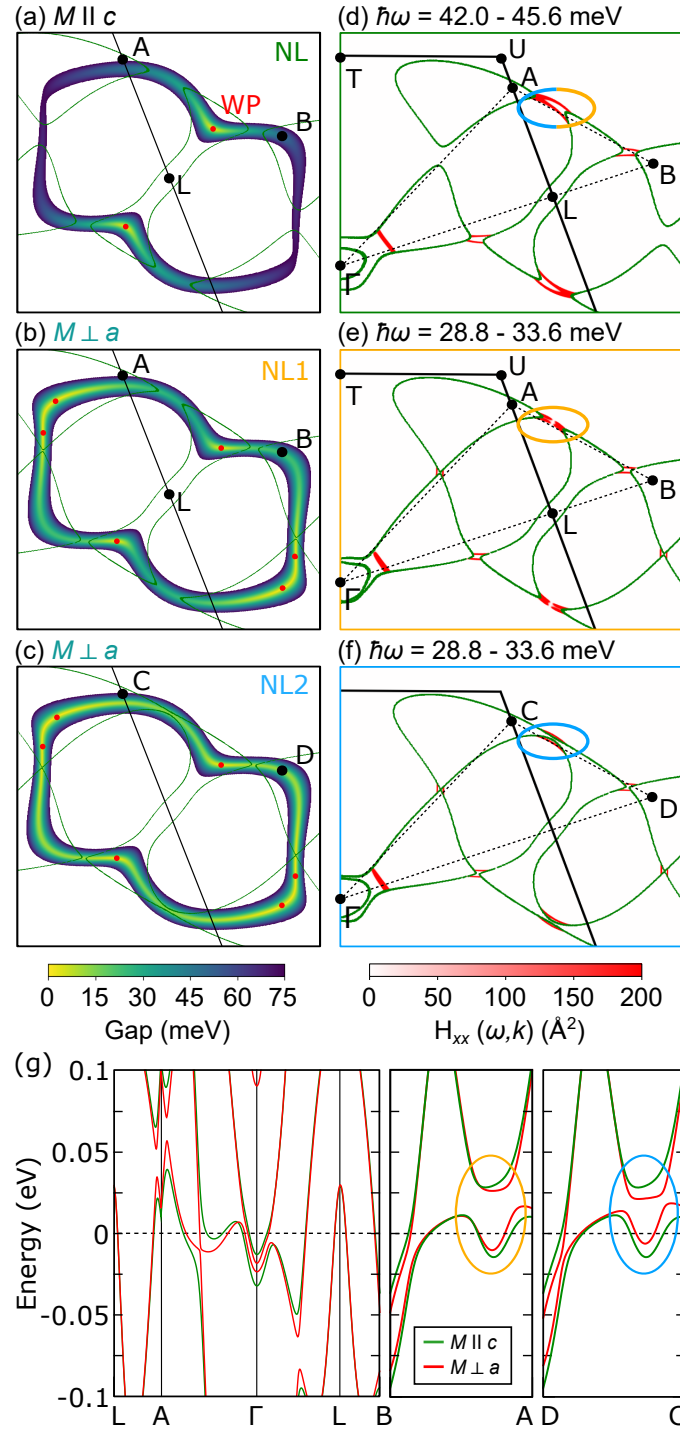


FIG. E4. Evolution of the nodal loop upon reorienting the magnetization to $\mathbf{M} \perp a$ (a-c) gap of the nodal lines for out-of-plane and NL1 and NL2 in-plane loops, respectively. For (a), the average gap is larger than for (b) and (c). Points C and D are equivalent to A and B but lie on the BZ planes that contain NL2 instead of NL1. (d-f) Optical weight H_{xx} at the peak energies (42.0–45.6 meV in (d), 28.8–33.6 meV in (e) and (f)) distributed on the high symmetry planes of the BZ containing the nodal loops from (a-c). We obtain qualitatively similar distributions despite the different energy ranges. (g) band structure along the triangles in the right column. The high symmetry points are shown above and in Fig. 1(d). For in-plane magnetization, the SOC gap along the nodal line is clearly smaller than for out-of-plane.

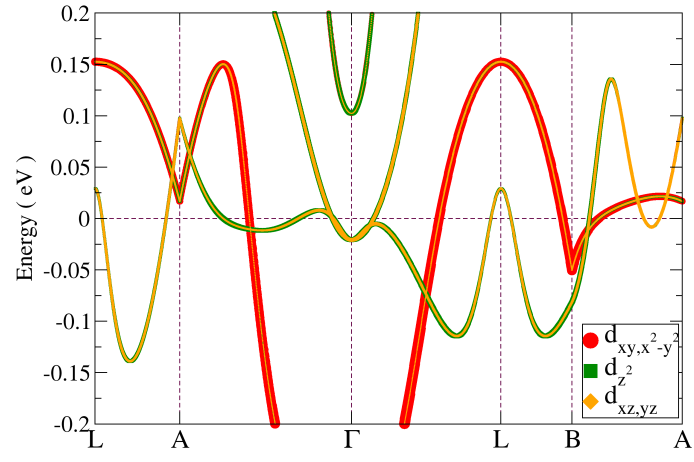


FIG. E5. Projected band structure of $\text{Co}_3\text{Sn}_2\text{S}_2$ at low energy and without the spin-orbit coupling.